

# Mechanical and Electrochemical Synergism of API X42 Pipeline Steel During Erosion–Corrosion

Md. Aminul Islam<sup>1</sup> · Zoheir N. Farhat<sup>1</sup>

Received: 26 June 2015 / Revised: 25 August 2015 / Accepted: 28 August 2015 / Published online: 11 September 2015  
© Springer International Publishing AG 2015

**Abstract** Hydro-transportation is an economic and flexible way to transport natural resources such as oil and gas from excavation to the extraction plants, refineries, and consumer-ready products to markets. However, interaction between solid particles, corrosive fluid, and target material often results in significant mutual reinforcement due to the combined action of erosion and corrosion. In this study, erosion–corrosion behavior of API pipeline steel has been assessed in  $2 \text{ g l}^{-1}$  NaCl solution purged with  $\text{CO}_2$  as the corrosive media and aluminum oxide as the erodent. Four different particle velocities (36, 47, 63, and  $81 \text{ m s}^{-1}$ ) were employed, while the angle of incidence was kept constant at  $90^\circ$ . The synergism between erosion and corrosion has been studied by means of a newly designed test approach to mitigate the limitations of the in situ method and to identify the effect of erosion on corrosion and vice versa. The corrosion process was monitored using potentiodynamic polarization and weight loss measurements. Total material loss rate and the components of erosion, corrosion, and their synergistic interactions have been determined. Scanning electron microscopy examination and experimental results show that there is an immense correlation between erosion and corrosion. Significant synergism was observed due to the interaction of different erosion and corrosion mechanisms.

**Keywords** Erosion–corrosion · Synergy · Electrochemical characterization · Erosion–corrosion mechanism · Particle velocity

## 1 Introduction

During the transportation of natural resources (oil and gas) metal surface is exposed to flowing corrosive environment, in which, the mechanical process of metal removal through erosion and the electrochemical process of corrosion are coupled [1–4]. Here the observed mass loss is higher than the summation of mass loss due to pure erosion and pure corrosion. The interaction between these two processes has been referred to by different researchers as ‘synergistic’ effect [5, 6]. Corrosion of carbon steel in  $\text{CO}_2$  environment is a continuing problem in oil and gas industries. As oil and gas emerge from geological formations they are often accompanied by water and varying amount of ‘acid gases’ such as carbon dioxide ( $\text{CO}_2$ ) and hydrogen sulfide ( $\text{H}_2\text{S}$ ). Several investigations [7–19] have been reported to study the erosion–corrosion phenomena involved.

The synergistic effect between erosion and corrosion has been receiving more and more attention in recent years because the mechanism of synergy is not thoroughly understood. Postlethwaite [20] pointed out that corrosion increases erosion rate by roughening the metal surface because erosion is sensitive to the impingement angle of solid particles. Matsumura et al. [21] proposed that the increase in the surface roughness plays a role in synergism and suggested that erosion can be enhanced by corrosion through the elimination of the work-hardened layer. Recently, Li et al. [1] proposed that localized attack causes disruptions in the surface oxide film (caused by particle impact), which enhances crack growth. Oxide flakes then detach leading to increased erosion. Hu and Neville [22] studied  $\text{CO}_2$  erosion–corrosion behavior of API X65 steel in oil and gas environment. They found that surface degradation due to corrosion process reduces the resistance to erosion. Burstein et al. [6] observed that corrosion rate

✉ Md. Aminul Islam  
Md.Aminul.Islam@Dal.Ca

<sup>1</sup> Department of Process Engineering and Applied Science, Materials Engineering Program, Dalhousie University, Halifax, NS B3J 2X4, Canada

doubled in the presence of erosion. This is because of the detachment of the flakes formed by repeated impacts of solid particles. This observation supports previous speculation [2, 23, 24] that erosion affect corrosion by increasing local turbulence/mass transfer and by surface roughening.

Erosion is very much dependent on the impacting particle properties (density, hardness, size, and shape), target material, particle feed rate, temperature, impact angle, and velocity of abrasive particles [25–40]. However, impact angle and particle velocity have been recognized as two parameters that remarkably influence erosion rates and surface degradation in tribo-systems. Lopez [41] studied the effect of abrasive velocity and concluded that surface damage increases with increasing impact velocity of the particles. Erosion rate has been shown [42–47] to follow an empirical power law relationship with velocity,

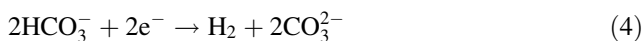
$$E = kV^n \quad (1)$$

where  $V$  is particle velocity,  $k$  is a constant, and  $n$  is the velocity exponent, and has values between 2 and 3.5 for metallic materials. It is believed that particle feed rate also plays an important role during erosion. The influence of the particle feed rate on erosion behavior has been investigated in the open literature [48–52].

Gas injection is presently the most commonly used approach in enhanced oil recovery. Carbon dioxide gas ( $\text{CO}_2$ ) is often injected in deep oil and gas wells because it reduces the oil viscosity and assists in the recovery effort [52–55]. The electrochemical corrosion behavior of carbon steel was studied in sweet environment where the presence of  $\text{CO}_2$  leads to the formation of a weak carbonic acid ( $\text{H}_2\text{CO}_3$ ) which drives the carbonate/bicarbonate ( $\text{CO}_3^{2-}/\text{HCO}_3^-$ ) corrosion reactions [56]. This initiating step is represented by the reaction,



The subsequent corrosion process is controlled by three cathodic reactions and one anodic reaction [56]. Cathodic reactions include the reduction of carbonic acid into bicarbonate ions, reduction of bicarbonate ions into carbonate ions, and the reduction of hydrogen ions to hydrogen gas.

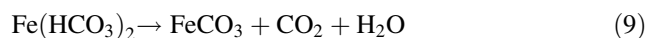
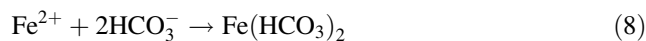
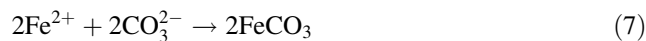


In carbonate/bicarbonate media, the anodic reaction involves oxidation of iron to ferrous ( $\text{Fe}^{2+}$ ) ion,



These corrosion reactions provide a chemical environment which promotes the formation of iron carbonate

( $\text{FeCO}_3$ ), where ferrous ions react directly with carbonate ions. Iron carbonate can also form by a two-step process: (i) ferrous ions react with bicarbonate ions to form iron bicarbonate; (ii) dissociation of iron bicarbonate into iron carbonate along with carbon dioxide and water [57].



The significance of  $\text{FeCO}_3$  formation is that it drops out of solution as a precipitate due to its limited solubility [57]. This precipitate has the potential to form passive film on the surface of the steel which reduces corrosion.

In order to identify the effect of corrosion on erosion and vice versa, it is important to separate the metal loss contributions due to erosion, corrosion, and their interactions. Various techniques [58, 59] have been used by different researchers to quantify these components which facilitate the analysis of material loss mechanisms and development of predictive models [60–64]. The total material loss during erosion–corrosion process can be defined as follows [65]:

$$T = E_0 + C_0 + S \quad (10)$$

where  $T$  is the total mass loss rate of the material,  $E_0$  is the erosion rate in absence of corrosion,  $C_0$  is the corrosion rate in absence of erosion, and  $S$  is the synergistic component and is defined as follows:

$$S = \Delta C_e + \Delta E_c \quad (11)$$

where

$$\Delta C_e = C_e - C_0 \quad (12)$$

$$\Delta E_c = E_c - E_0 \quad (13)$$

$\Delta C_e$  is the change in corrosion rate due to erosion and  $\Delta E_c$  is the change in erosion rate due to corrosion,  $E_c$  is the total erosion component in the presence of corrosion, and  $C_e$  is the total corrosion component in the presence of erosion. It is important to note that erosion–corrosion mass loss can sometime also be lower than the summation of mass loss due to pure erosion and pure corrosion. In that case, the effect is called the antagonistic effect or negative synergism [66].

Depending upon the specific pipeline operating conditions and field environment, abrasive particle feed rate may vary from 0.03 to 24  $\text{g min}^{-1} \text{mm}^{-2}$  [67, 68]. In this study, relatively high particle feed rate was used in an attempt to reproduce actual operating conditions encountered in desert environment, where pipelines are subjected to erosion by high sand flux. Such conditions are common in middle-east oil and gas fields. The lack of such study has motivated the authors to conduct erosion–corrosion tests at high abrasive feed rate (mean value of 24  $\text{g min}^{-1} \text{mm}^{-2}$ )

to investigate the degradation behavior of API X42 steel under such condition. This study primarily focuses on understanding the erosion–corrosion mechanisms of API X42 pipeline steel and the constitutions of total material loss in terms of erosion, corrosion, and their interactions. In addition, some key parameters (morphology, nature, formation, and fracture of the surface film) affecting erosion–corrosion of API X42 steel in sweet environment are briefly presented. A newly designed test approach was used to avoid the fluctuation in electrochemical measurements due to bubble formation and turbulence associated with in situ measurements. It also provides better insight on the effect of erosion mechanism on corrosion and vice versa. Although the environmental conditions that the pipeline materials are exposed to in real application are different from laboratory monitoring systems, the objective of current work is to improve the understanding of erosion–corrosion predictions by identifying critical parameters to ensure effective use of API X42 steel in oil and gas production.

## 2 Experimental

### 2.1 Materials

API X42 steel coupons (15.8 mm diameter and 4.7 mm thick) were used as test specimens and aluminum oxide particles were used as erodent in all erosion and corrosion experiments. The physical and chemical properties of the specimen and the erodent are given in Table 1.

### 2.2 Surface Characterization

API X42 specimens were ground using 240, 320, 400, and 600 grit SiC abrasive papers and then polished using 1, 0.3, and 0.05 μm gamma alumina suspension prior to experiments.

Figure 1 shows the microstructure and XRD pattern of API X42 steel. The micrograph in Fig. 1 (a) reveals a mixture of proeutectoid ferrite (86 %) and pearlite (14 %) as expected in API X42. The grains are regular, having an average size of  $10 \pm 2 \mu\text{m}$ . XRD peaks (Fig. 1b) were matched to those in the Powder Diffraction Files (PDF) and identified as carbon steel peaks having a BCC crystal structure. Malvern mastersizer 3000 laser diffraction particle size analyzer was used to measure the particle size distribution of the aluminum oxide erodent. The technique follows ISO 13320:2009 standard [69]. The abrasive particle size distribution is shown in Fig. 2a. These results give a mode of about  $63 \pm 3 \mu\text{m}$  and an average abrasive particle size of about  $57 \pm 3 \mu\text{m}$ . SEM image of the alumina erodent reveals irregular angular shaped particles as shown in Fig. 2b.

### 2.3 Experimental Setup

#### 2.3.1 Erosion Test

An erosion tester designed to control and adjust particle impact velocity, particle flux, and specimen distance and orientation relative to the impinging abrasive stream was used. The tester is similar to those used by other researchers for studying solid particle erosion [67, 70–72]. Figure 3 shows a schematic diagram of the dry erosion tester [73, 74].

Operating conditions for erosion tests are given in Table 2. The abrasive particle velocity range used in this study was  $36\text{--}81 \text{ m s}^{-1}$  (Table 2). In this study, particle velocity was measured as a function of air pressure using double-disk method [72]. Calibration curve for air jet pressure vs particle velocity was reported in a previous study [74]. The ASTM standard [69] recommends a particle velocity of  $30 \text{ m s}^{-1}$ . However, different researchers have used different particle velocities in their studies. For example, Ruff and Ives [72] have used  $71\text{--}88 \text{ m s}^{-1}$

**Table 1** Physical and chemical properties of API X42 and aluminum oxide

API X42 steel										Aluminum oxide						
Yield strength	290 MPa									Crystal phase	Alpha					
Elongation	23 %									Specific gravity	3.95 g cm <sup>-3</sup>					
Density	7.84 g cm <sup>-3</sup>									Melting point	2000 °C					
Vickers hardness	1.34 GPa									Hardness	27.13 GPa					
Grain size	10 ± 2 μm									Particle size	57 ± 3 μm					
Composition of API X42 (wt.%)										Composition of aluminum oxide (wt.%)						
Fe	C	Mn	P	S	Si	Cr	Ti	V	Nb	AlO <sub>2</sub>	TiO <sub>2</sub>	SiO <sub>2</sub>	Fe	MgO	Alkali	
balance	0.169	0.372	0.040	0.004	0.067	.0027	0.002	0.001	<0.001	99.5	0.099	0.05	0.08	0.02	0.30	

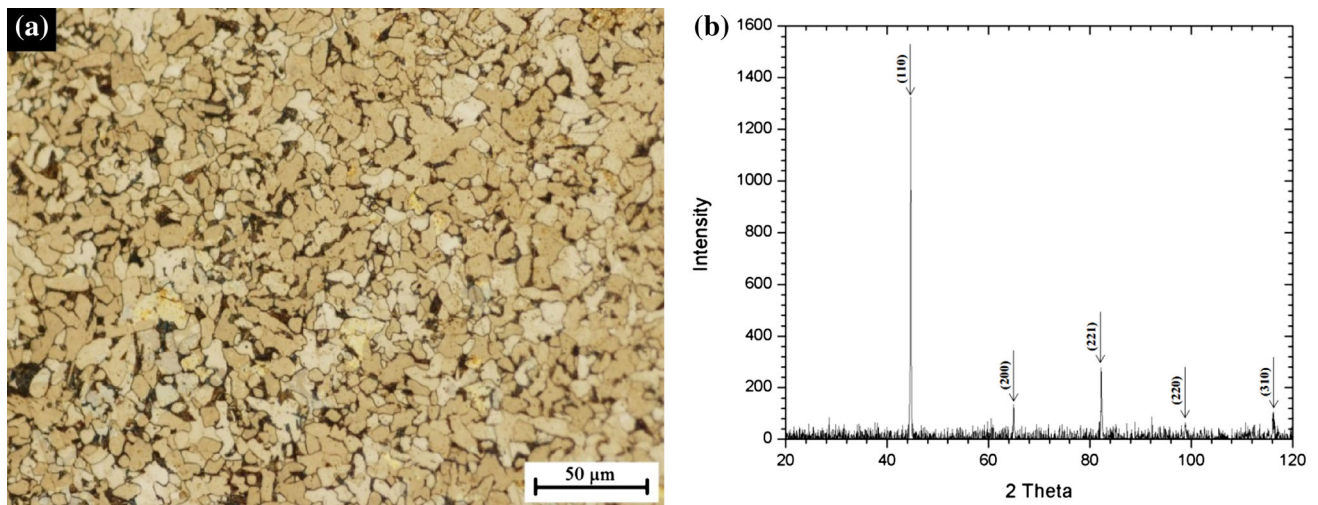


**Fig. 1** **a** Optical micrograph of API X42 showing a mixture of proeutectoid ferrite (86 %) and pearlite (14 %) and **b** XRD pattern of API X42 steel identified as carbon steel peaks having a BCC crystal structure

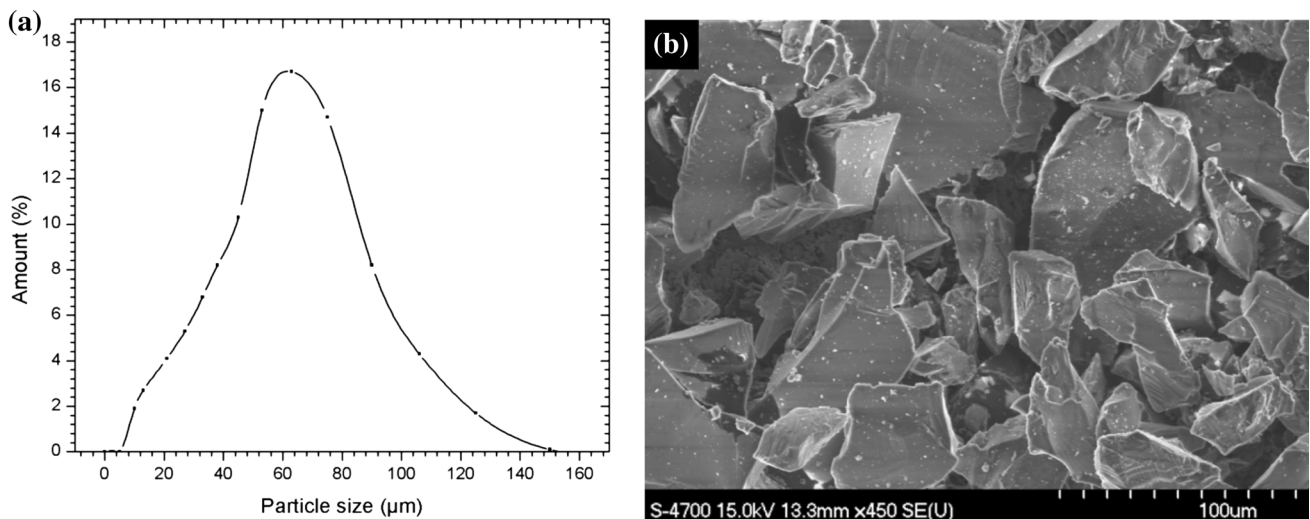


**Fig. 2** **a** Particle size distribution of alumina abrasive having an average particle size of  $57 \pm 3 \mu\text{m}$  and **b** SEM micrograph of the alumina abrasive showing irregular shaped particles

particle velocity range. Other researchers [70, 71] have also used higher particle velocities than stated in the ASTM standard. In this study, a wide range of particle velocity was used in order to assess the effect of particle velocity on erosion and corrosion. Specimens were weighed using a digital balance (with an accuracy of  $1 \times 10^{-5}$  g) before and after each erosion test. Erosion rate in the absence of corrosion ( $E_0$ ) ( $\mu\text{m s}^{-1}$ ) was calculated using the following equation [65]:

$$E_0 = \left[ \frac{\Delta W}{A dt} \right] K_1 \quad (14)$$

where  $\Delta W$  is the weight loss (g) of the specimen,  $A$  is the projected eroded surface area ( $\text{mm}^2$ ),  $d$  is the density

( $\text{g cm}^{-3}$ ),  $t$  is test duration (s), and  $K_1$  is a constant ( $1 \times 10^6 \mu\text{m cm}^{-1}$ ).

## 2.4 Corrosion Test

A conventional three-electrode electrochemical glass cell with a graphite counter electrode and a saturated calomel electrode (SCE) (reference) [75] was used for electrochemical measurements. All potentials are reported in SCE scale. Polarization curves were generated by changing the electrode potential using a Uniscan potentiostat PG581, at a sweep rate (scan rate) of  $0.166 \text{ mV s}^{-1}$ . Prior to electrochemical tests, the working electrode was kept in the solution and allowed to attain a stable open circuit potential

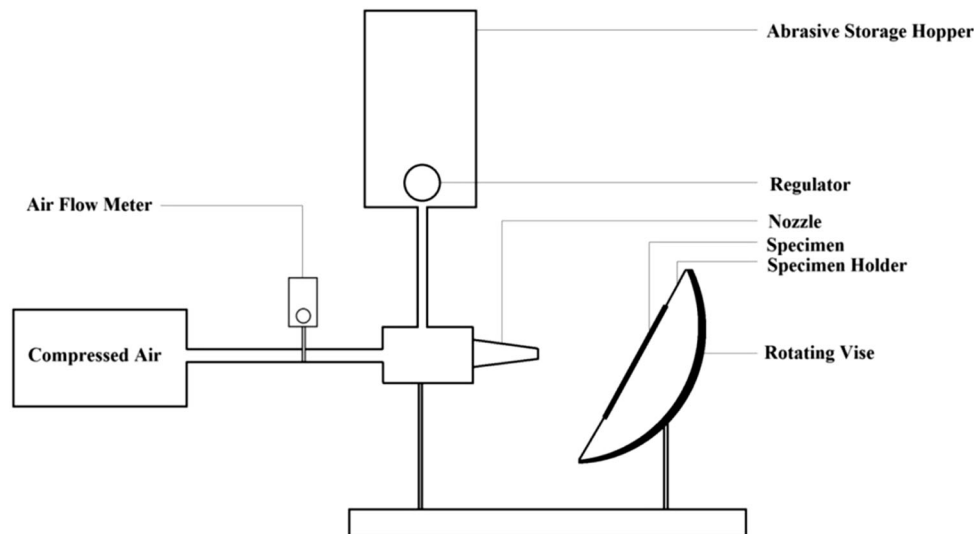


**Fig. 3** Schematic diagram of the erosion tester showing rotating angular vise, specimen holder, abrasive storage hopper, and air flow meter [73, 74]

**Table 2** Operating conditions for pure erosion tests of API X42 steel

Parameter	Operating condition
Nozzle diameter	2.3 mm
Projected eroded surface area	8.66 mm <sup>2</sup>
Standoff distance	3 mm
Test gas	Dry compressed air
Test duration	50 s
Test temperature	Ambient
Angle of incidence	90°
Particle velocity	36, 47, 63 and 81 m s <sup>-1</sup>

(OCP). Measurements indicate that a stable OCP for API X42 steel was achieved after 1.5 h of immersion. After stabilization, potentiodynamic polarization curves were generated by changing the working electrode potential from an initial value of 250 mV below OCP up to 250 mV above OCP.

Corrosion tests were conducted in one liter solution containing 2 g NaCl (0.03 M). CO<sub>2</sub> gas was purged through the cell until saturation. At saturation, the pH of the solution reached a value of 4.3. The flow of CO<sub>2</sub> was turned off during the experiment to avoid turbulence or gas bubble formation at the surface of the specimen. The pH of CO<sub>2</sub> saturated solution was monitored continuously during corrosion tests and was maintained at a constant value of 4.3 throughout the experiments. All tests were performed at the ambient temperature. Specimens were weighed before and after each corrosion test. Corrosion rate in absence of erosion ( $C_0$ ) ( $\mu\text{m s}^{-1}$ ) based on weight loss was calculated using the following equation [65]:

**Table 3** Operating conditions for pure corrosion tests of API X42 steel

Parameter	Operating condition
Test solution	1 liter distilled water + 2 g NaCl
Corroded surface area	100 mm <sup>2</sup>
Test duration	2.5 h
Test temperature	Ambient
Sweep rate	0.166 mV s <sup>-1</sup>
Potentiodynamic sweep	From -250 to 250 mV (vs OCP)
pH	4.3
Pressure	100 kPa CO <sub>2</sub>
Velocity	Stagnant

$$C_0 = \left[ \frac{\Delta W}{A dt} \right] K_2 \tag{15}$$

where  $\Delta W$  is the weight loss (g) of the specimen,  $A$  is the surface area (mm<sup>2</sup>),  $d$  is the density (g cm<sup>-3</sup>),  $t$  is test duration (h), and  $K_2$  is a constant (277.78  $\mu\text{m h cm}^{-1} \text{s}^{-1}$ ).

Corrosion rate in the absence of erosion ( $C_0$ ) ( $\mu\text{m s}^{-1}$ ) based on potentiodynamic polarization corrosion current ( $I_{\text{corr}}$ ) was calculated using the following equation [65]:

$$C_0 = \frac{K_3 I_{\text{corr}} EW}{d} \tag{16}$$

where  $K_3$  is a constant ( $1.03 \times 10^{-7} \mu\text{m g } \mu\text{A}^{-1} \text{cm}^{-1} \text{year}^{-1}$ ),  $I_{\text{corr}}$  is the corrosion current density ( $\mu\text{A cm}^{-2}$ ), and  $EW$  is the equivalent weight and  $d$  is the density (g cm<sup>-3</sup>). The operating conditions for corrosion tests are given in Table 3.

## 2.5 Erosion–Corrosion Test

Different researchers have used different test facilities to simulate erosion–corrosion of steels in CO<sub>2</sub> environment with abrasive particles. Shadley et al. [76, 77] constructed a mini loop composed of a diaphragm pump, a test section, a cyclone separator, a sand injector, and a sump. A CO<sub>2</sub> saturated test solution was circulated by the pump. Sand was injected into the liquid at the sand injector below the cyclone separator and carried into the test section by the circulating solution. Test cell was connected to a potentiostat with reference and counter electrodes and linear polarization measurements were performed to determine whether and when FeCO<sub>3</sub> corrosion product forms. Neville et al. [22, 78–81] used an impinging jet apparatus (recirculation rig) coupled with an electrochemical setup in a sealed vessel for erosion–corrosion study. To determine material loss due to pure erosion, the test solution was prepared using tap water and N<sub>2</sub> was bubbled through the solution to reduce oxygen content. During erosion–corrosion, test solution (NaCl + water) was purged with CO<sub>2</sub> before experiments. Stack et al. [66, 82] constructed an apparatus consisting of a large plastic tank that was used as a chamber. The solution was delivered with high pressure through a flex vent. When the solution entered the ejector at high speed, it produced a partial vacuum due to venturi effect and the slurry underneath the tube was mixed with the flowing solution by means of suction. An electrochemical cell was incorporated into the test rig to enable in situ electrochemical tests and to control the potential of the specimen. The erosion–corrosion rate was obtained by mass loss techniques, while corrosion contribution, during the erosion–corrosion process was estimated by integration within the area under the current–time curve. Wood et al. [83, 84] performed erosion–corrosion experiments in a slurry pot erosion tester driven by a motor. The rig assembly was enclosed within a Faraday cage which allows electrochemical measurements. For pure erosion experiments, 0.1 M NaOH was used as the test solution with the addition of silica sand. Pure corrosion experiments were performed using 3.5 % NaCl. Erosion–corrosion experiments were performed using similar corrosive solutions as used in pure corrosion with the addition of silica sand. Xie et al. [85] showed that by increasing frequency of the intermittent erosion–corrosion cycle, it is possible to obtain close results as if erosion and corrosion happened together. This test method provides more stable electrochemical measurements and is employed to mitigate the limitations of the in situ method [22, 24], including the difficulty of controlling fluctuation in electrochemical data due to bubble formation and turbulence.

In this study, in order to calculate the rate of material loss contributions from erosion, corrosion, and their

interactions, specimens were subjected to erosion for 10 s and erosion rate was calculated using Eq. 14. Eroded specimens were then subjected to corrosion for 2.5 h and corrosion rate was then calculated from both potentiodynamic polarization (Eq. 16) and weight loss (Eq. 15). In the present work, erosion followed by corrosion is termed ‘cycle.’ Five erosion–corrosion cycles (starting with erosion and finishing with corrosion) were performed, which gives a total of 50 s of erosion and 12.5 h of corrosion. Total erosion component ( $E_c$ ) and total corrosion component ( $C_c$ ) are averages of five consecutive erosion and corrosion cycles, respectively. Erosion rate in the absence of corrosion ( $E_0$ ) and corrosion rate in the absence of erosion ( $C_0$ ) were calculated from pure erosion for 50 s and pure corrosion for 12.5 h, respectively. The increase in material loss rate was then calculated using Eqs. 10–13. It is worth noting that erosion and corrosion tests in this study were not performed simultaneously. The synergistic effect of erosion–corrosion in this work refers to the result of the cyclic erosion and corrosion tests.

The surface ( $A_3$ ) of the specimen exposed to erosion and corrosion is calculated using the following equation:

$$A_1 = A_2 + A_3 \quad (17)$$

where  $A_1$  = entire surface of the specimen exposed to corrosion and  $A_2$  = surface area exposed to corrosion only. The corrosion current density ( $I_{\text{corr},A_2}$ ) contribution from  $A_2$  surface area is calculated from pure corrosion (potentiodynamic polarization) experiment using the following equation:

$$I_{\text{corr},A_2} = \frac{I_{\text{corr}}A_2}{A_1} \quad (18)$$

where  $I_{\text{corr}}$  is the corrosion current density ( $\mu\text{A cm}^{-2}$ ) during pure corrosion from the entire surface area ( $A_1$ ). During erosion–corrosion experiment,  $I_{\text{corr}}^*$  (corrosion current density during erosion–corrosion) calculated from potentiodynamic data has contributions from both pure corrosion ( $A_2$ ) and erosion–corrosion ( $A_3$ ) areas. Therefore, erosion enhanced corrosion current density ( $I_{\text{corr},A_3}$ ) can be calculated using the following equation:

$$I_{\text{corr},A_3} = I_{\text{corr}}^* - I_{\text{corr},A_2} \quad (19)$$

Erosion enhanced corrosion rate is then calculated using Eq. 16. During erosion–corrosion, entire surface area ( $A_1$ ) exposed to corrosion, surface area ( $A_2$ ) only exposed to corrosion and surface area ( $A_3$ ) exposed to both erosion–corrosion are 100, 91.34, and 8.66 mm<sup>2</sup>, respectively. The operating conditions for erosion–corrosion experiments are given in Table 4.

To investigate the sub-surface of the erosion scar, specimens were cross sectioned using a Buehler<sup>®</sup> isomet 1000 precision saw having diamond wafering blade

**Table 4** Operating condition for erosion–corrosion of API X42 steel

Erosion		Corrosion	
Nozzle diameter	2.3 mm	Test solution	1 liter distilled water + 2 g NaCl
Standoff distance	3 mm	Sweep rate	0.166 mV s <sup>-1</sup>
Test gas	Dry compressed air	Potentiodynamic sweep	From -250 to 250 mV (vs OCP)
Test duration	10 s for each cycle	Test duration	2.5 h for each cycle, 12.5 h for pure corrosion
Number of cycles	5	Number of cycles	5
Test temperature	Ambient	pH	4.3
Angle of incidence	90°	Pressure	100 kPa CO <sub>2</sub>
Particle velocity	36, 47, 63 and 81 m s <sup>-1</sup>	Velocity	Stagnant

(15.2 cm dia. × 0.5 cm thick). In order to avoid excessive heating and plastic deformation, specimens were cut using a small load of 50 g and low speed of 100 rpm. Buehler® isocutplus cutting fluid was mixed with water (1:9) and used as a coolant to prevent heating produced during cutting.

Worn surfaces were examined using a Hitachi S-4700 scanning electron microscope to determine possible material removal mechanisms operating under different test conditions.

### 3 Results and Discussion

#### 3.1 Erosion

During pure erosion, API X42 steel was exposed to abrasive stream for 50 s at 90° angle of incidence and different particle velocities (36, 47, 63, and 81 m s<sup>-1</sup>). Erosion rate in the absence of corrosion ( $E_0$ ) was calculated using

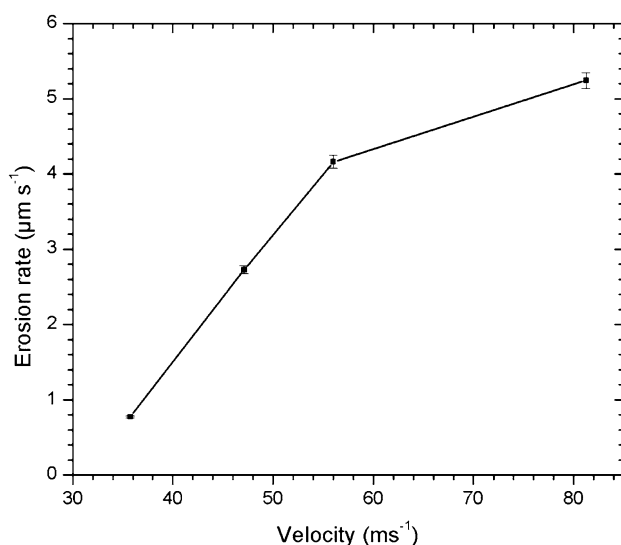


**Fig. 4** Erosion rate vs abrasive particle velocity for API X42 steel showing an increase in erosion rate with particle velocity

Eq. 14 and is plotted in Fig. 4. It should be noted that error bars in plots in the present work represent standard deviations of several measurements made per data point. As expected, higher particle velocity leads to higher material removal from the surface as observed in other erosion studies [86]. This is because of the fact that higher particle velocity is associated with higher kinetic energy which leads to more material removal. It is believed that when the particle velocity is low, hence, low kinetic energy, only small fraction of the abrasive particles have high enough velocity and mass to cause plastic deformation to the steel surface. The majority of particles have low energy below a threshold value, which only results in elastic deformation of the steel. As particle velocity increases, more particles attain the required critical energy to result in plastic deformation and material removal. That is, at low particle velocity, most of the impact is elastic and does not contribute to the measured erosion rate. In order to quantify the velocity exponent  $n$  (Eq. 1), erosion rate data in Fig. 4 were curve fit using nonlinear least square method. It was found that during pure erosion of API X42 steel (50 s test duration), the velocity exponent  $n$  has a value of 2.13.

Erosion is a complex time-dependent phenomena. Different erosion mechanisms operate simultaneously and interact with one another, which makes the identification of these mechanisms a challenging task. Contributions from different mechanisms control the net erosion rate of the material. At low particle velocity (36 m s<sup>-1</sup>), most of the abrasive particle kinetic energy is used to penetrate the surface and form dimples by locally micro-forge the surface and, in the process, form work-hardened layer due to plastic deformation (Fig. 5a). A number of other investigators have also reported the formation of a work-hardened layer during erosion [87–89]. For example, Levy believed that a work-hardened region results from extensive plastic deformation occurring just below the surface [88]. Papini [53] showed that low erosion rate at 90° impact angle was likely due to a significantly hardened surface layer since the energy transfer normal to the surface was at its maximum. During impact the metal is squeezed out of the

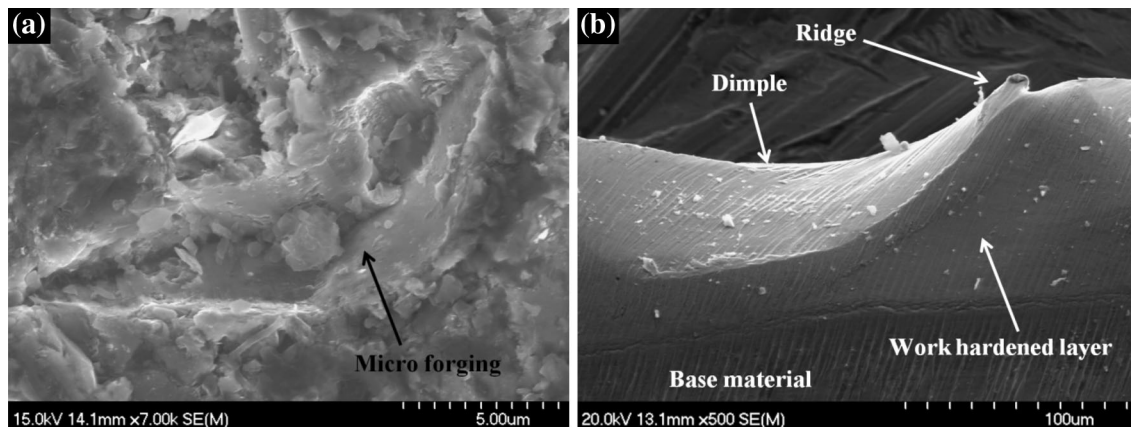


**Fig. 5** SEM micrograph of the steel specimen after erosion, **a** micro-forging of the surface by the abrasive particle, and **b** cross-sectional image of the erosion scar showing the formation of work-hardened layer and dimple and ridge formation on the eroded surface

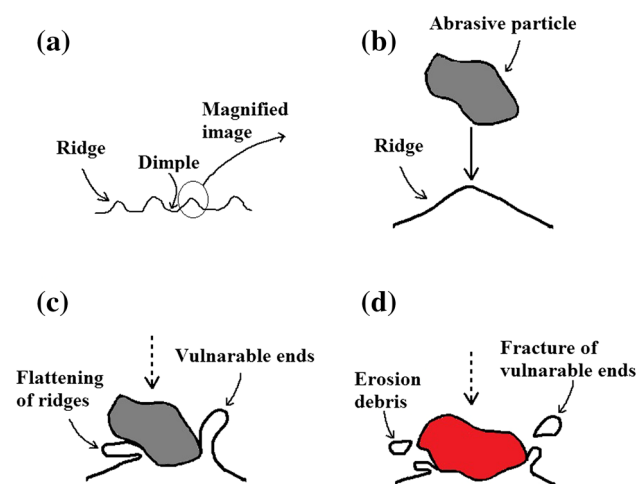


**Fig. 6** Schematic diagram illustrates the stages of metal removal. **a–b** Metal is squeezed out of the dimples to form ridges, which are then removed by fracture (**c–d**) due to plastic deformation and flattening of ridges around dimples

dimples due to plastic deformation to form ridges. The cross section of the erosion scar (Fig. 5b) shows the formation of ridges and work-hardened layer. Material removal occurs by fracture and flattening of ridges around dimples. A schematic diagram (Fig. 6) illustrates the stages of metal removal by this mechanism. Figure 6a shows the formation of ridges and dimples on the eroded surface due to repeated impact by abrasive particles. Figure 6b–d are magnified images of Fig. 6a, which illustrate the removal of ridges due to plastic deformation and fracture caused by the abrasive particles impact. This process of metal removal is observed at low particle velocity and more so at high velocity.

During erosion,  $\text{Al}_2\text{O}_3$  particles are observed to embed into the steel surface (Fig. 7a), which has also been identified in earlier studies [72, 73, 90]. At high particle

velocity ( $81 \text{ m s}^{-1}$ ), embedded  $\text{Al}_2\text{O}_3$  undergo repeated impact by the incoming particle stream which leads to particle fracture (Fig. 7b). Fractured particles are then removed from the surface leaving behind vulnerable lips (Fig. 7c). Material removal typically involves the flattening of a protrusion (lips) and fracture upon subsequent impact. The higher the impact velocity, the deeper the abrasive particles penetrate into the matrix, hence, more material removal. This metal removal process seems to dominate under conditions of high particle velocity. Earlier studies [91–93] showed that in a multiple impact situation, lips are initially formed by extrusion of surface material from earlier impact. These lips are fragile in nature and may not be removed immediately but would easily be removed by subsequent impact by another particle. In addition, metal cutting is also observed (Fig. 7d) and contributes to metal loss. Metal cutting is usually observed at high particle velocity where  $\text{Al}_2\text{O}_3$  particles strike and deflect by previously embedded particles and erode a small portion of metal ( $2\text{--}3 \mu\text{m}$ ). Metal cutting mechanism has been described elsewhere [73].

### 3.2 Corrosion

A typical potentiodynamic polarization curve for API X42 steel in  $2 \text{ g l}^{-1}$  NaCl in the presence of  $\text{CO}_2$  is given in Fig. 8. The corrosion current density ( $I_{\text{corr}}$ ) of the system was measured from Tafel extrapolation. Statistical analysis was performed to measure the accuracy of the fit, which gives a  $p$  value of 0.003. It indicates that the accuracy of the fit is at 95 % confidence level. The corrosion current density, anodic ( $\beta_a$ ), and cathodic ( $\beta_c$ ) Tafel slopes are  $52.5 \mu\text{A cm}^{-2}$ ,  $79.2 \text{ mV decade}^{-1}$ , and  $-507.2 \text{ mV decade}^{-1}$ , respectively. Corrosion rate is calculated (Eq. 16) to be  $1.93 \times 10^{-5} \mu\text{m s}^{-1}$ . The specimen was weighed before and after the corrosion test and the corrosion rate calculated



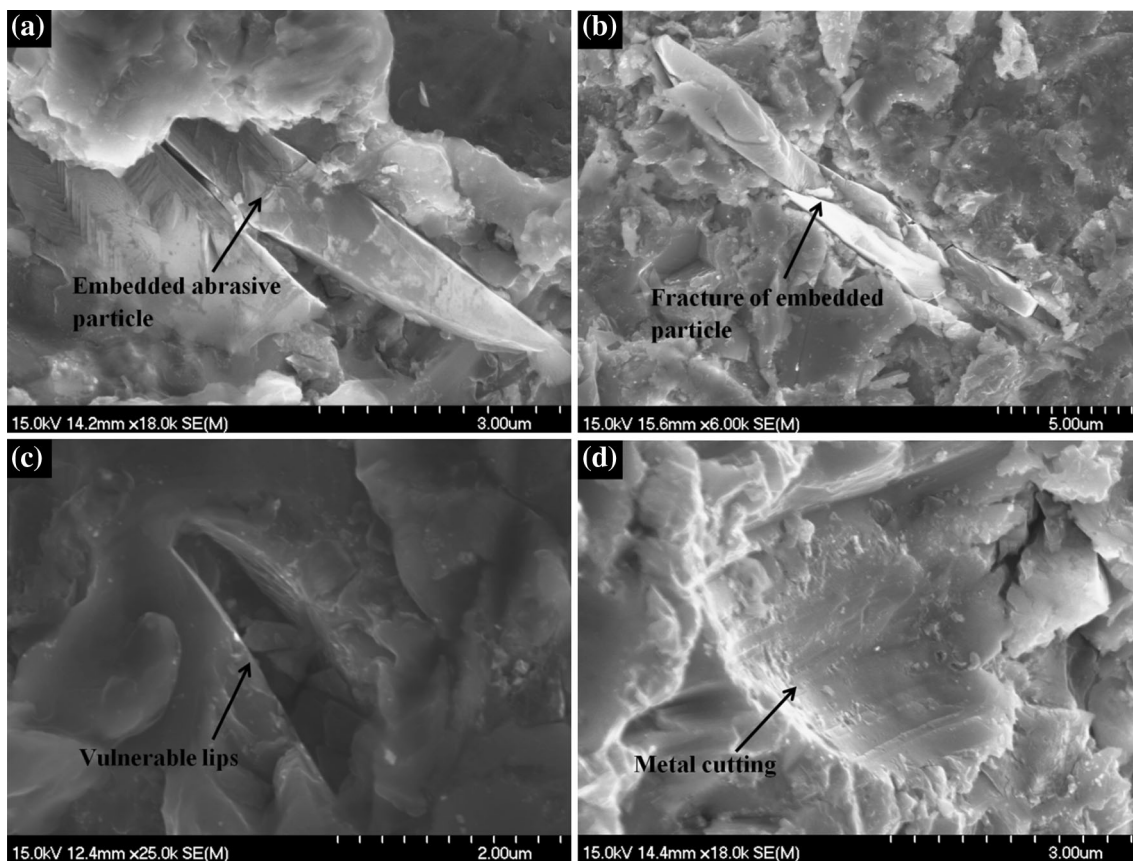


**Fig. 7** SEM micrograph of a specimen after pure erosion, **a** embedded Al<sub>2</sub>O<sub>3</sub> particle, **b** fracture of embedded particle due to repeated impact by the imminent particle stream, **c** formation of vulnerable lips

due to the removal of embedded particle, and **d** metal cutting caused by the abrasive particle

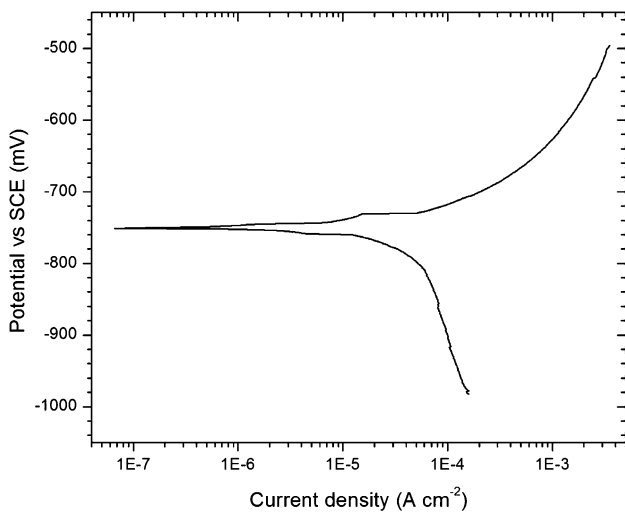


**Fig. 8** Potentiodynamic polarization curve for API X42 steel in 2 g l<sup>-1</sup> NaCl saturated with CO<sub>2</sub> at a pH of 4.3. Corrosion current density was measured from Tafel extrapolation

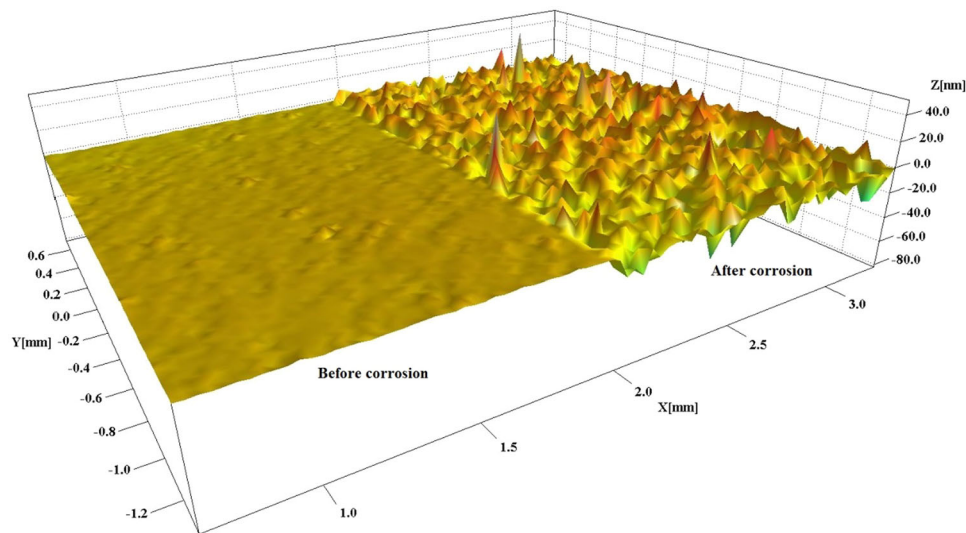
from weight loss (Eq. 15) is  $4.39 \times 10^{-5} \mu\text{m s}^{-1}$ . Table 5 summarizes the data obtained from pure corrosion experiment.

Profilometry scans were performed before and after corrosion of API X42 steel samples. Scanned profiles were then stitched together for comparison as shown in Fig. 9. The surface roughness of the specimen was measured and is tabulated in Table 6. It was found that there is around 54 % increase in surface roughness after corrosion.

Figure 10a shows SEM micrograph of etched as-received API X42 steel. As described earlier, API X42 consists of ferritic (86 %) and pearlitic (14 %) microstructure having an average grain size of  $10 \pm 2 \mu\text{m}$ . Figure 10b shows the magnified image (marked as circle) of Fig. 10a illustrating the pearlitic and proeutectoid ferritic microstructure before corrosion. The pearlitic microstructure of the steel after it was exposed to the corrosive solution (2 g l<sup>-1</sup> NaCl saturated with CO<sub>2</sub>) for 12.5 h is shown in Fig. 10c. It is generally agreed that ferrite is anodic to cementite (Fe<sub>3</sub>C) in CO<sub>2</sub> environment [94, 95], which leads to the dissolution of eutectoid ferrite into Fe<sup>2+</sup> ion and leaving behind a cementite (Fe<sub>3</sub>C) network in pearlite (Fig. 10c). It is believed that depending upon the morphology of these cementite (Fe<sub>3</sub>C) networks, they can reinforce a protective layer by anchoring it to the

**Table 5** Potentiodynamic polarization data for API X42 steel

	pH	$E_{\text{corr}}$ mV versus SCE	$I_{\text{corr}}$ ( $\mu\text{A cm}^{-2}$ )	Anodic beta ( $\beta_a$ ) (mV decade $^{-1}$ )	Cathodic beta ( $\beta_c$ ) (mV decade $^{-1}$ )	Corrosion rate from $I_{\text{corr}}$ ( $\mu\text{m s}^{-1}$ )	Weight loss (g mm $^{-2}$ )	Corrosion rate from weight loss ( $C_0$ ) ( $\mu\text{m s}^{-1}$ )
NaCl solution with CO $_2$	4.3	-754.2	52.5	79.2	-507.2	$1.93 \times 10^{-5}$	$3.1 \times 10^{-6}$	$4.39 \times 10^{-5}$

**Fig. 9** Profilometry scans of API X42 steel showing surface roughness profiles before and after pure corrosion**Table 6** Roughness data for API X42 steel before and after pure corrosion

	Before corrosion (nm)	After corrosion (nm)	% increase
Average roughness	$847 \pm 5$	$1306 \pm 5$	54
Root mean square	$1081 \pm 5$	$1674 \pm 5$	54

steel surface [96]. Again, anodic reaction involving oxidation of iron to ferrous ion in the corrosive solution leading to the preferential dissolution of proeutectoid ferrite as shown by the wavy appearance in Fig. 10d. The dissolution of iron provides a suitable chemical environment for the formation of iron carbonate ( $\text{FeCO}_3$ ), which then precipitates at the steel surface due to its limited solubility [57, 95, 97–100]. Figure 11 shows the EDS analysis performed on the specimen before and after corrosion. An order of magnitude increase in carbon to iron concentration ratio and the presence of high oxygen content indicate the possibility of the formation of  $\text{FeCO}_3$  on the corroded surface. The properties of the  $\text{FeCO}_3$  layer play an important role in determining the corrosion rate of the steel. In general, it acts as a diffusion barrier covering the underlying metal and decreasing the corrosion rate by preventing electrochemical reactions at the surface [101]. The protectiveness of such corrosion layer determines the long-term corrosion performance.

### 3.3 Erosion–Corrosion

During erosion–corrosion process, five erosion cycles (10 s each) were performed during cyclic erosion and corrosion tests for a total of 50 s of erosion time (same duration as pure erosion) for 36, 47, 63, and 81 m s $^{-1}$  particle velocity and 90° impingement angle. Figure 12 shows changes in average erosion rate with particle velocity in which each data point is an average of five erosion cycles. Depending upon the corrosion mechanisms involved in each cycle, erosion rate varies (within a narrow range) for the same particle velocity. The variation range is more pronounced at higher velocity. As shown in the figure, erosion rate increases with increasing particle velocity as observed previously for pure erosion (Fig. 4). The average erosion rate data in Fig. 12 were curve fit using nonlinear least square method, and it was found that during erosion–corrosion of API X42 steel, the velocity exponent  $n$  has a value of 2.03.

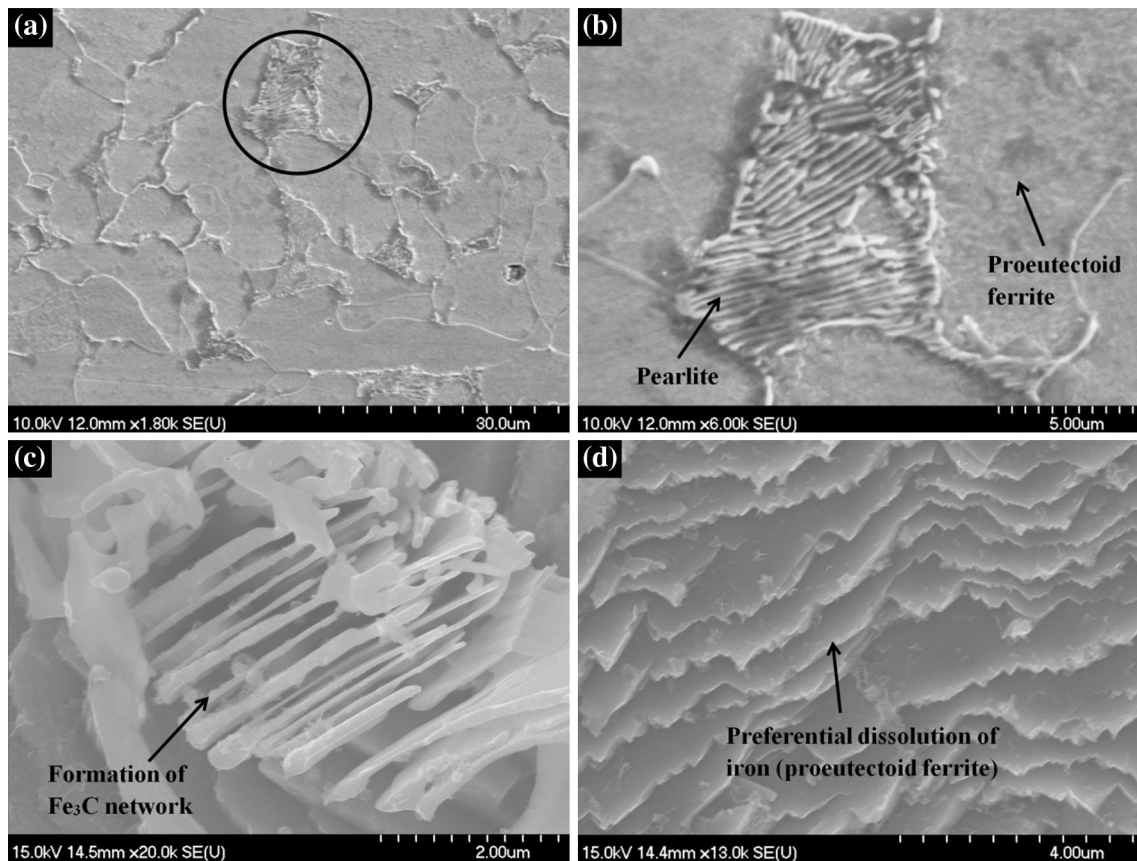


**Fig. 10** SEM images of **a** as-received API X42 steel after etching, **b** pearlite and proeutectoid ferrite before corrosion, **c** formation of cementite network due to the dissolution of eutectoid ferrite, and **d** preferential dissolution of proeutectoid ferrite

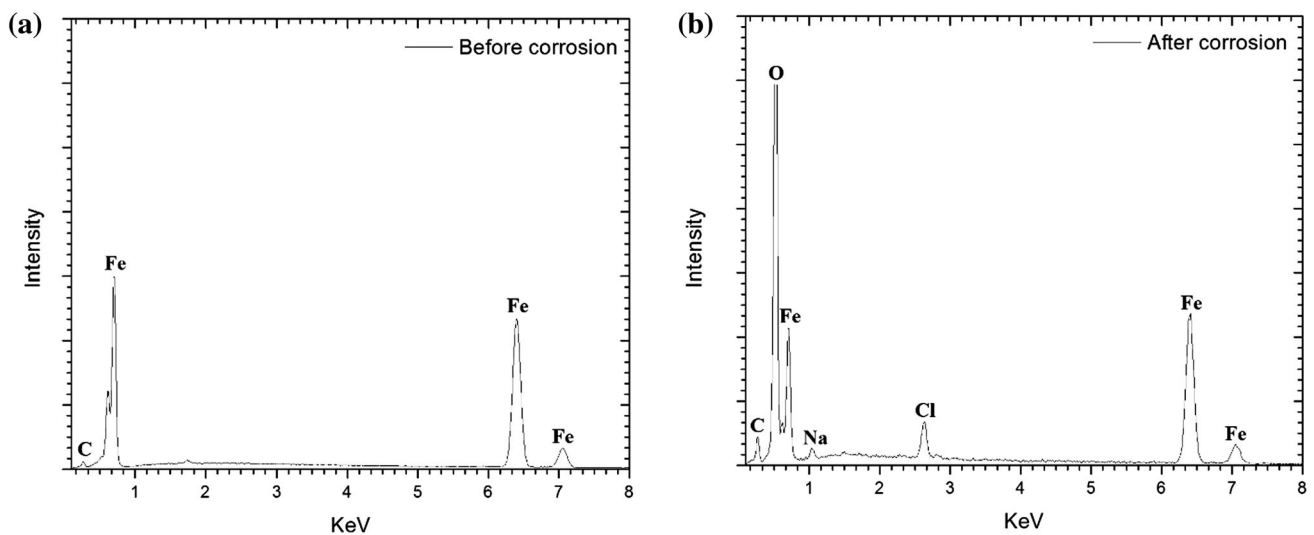


**Fig. 11** EDS analysis performed on the specimen **a** before corrosion and **b** after corrosion

On the other hand, Fig. 13 shows the average corrosion rate (corrosion of the eroded surface) of 5 cycles for each particle velocity. As shown in the figure, corrosion rate increases with increasing particle velocity. Abrasive particles partially or completely remove the protective surface

film and expose the fresh surface for further corrosion. High particle velocity results in more protective film removal from the surface. Partial removal of the protective surface film creates favorable condition for accelerated corrosion. Again, as observed from pure erosion, high

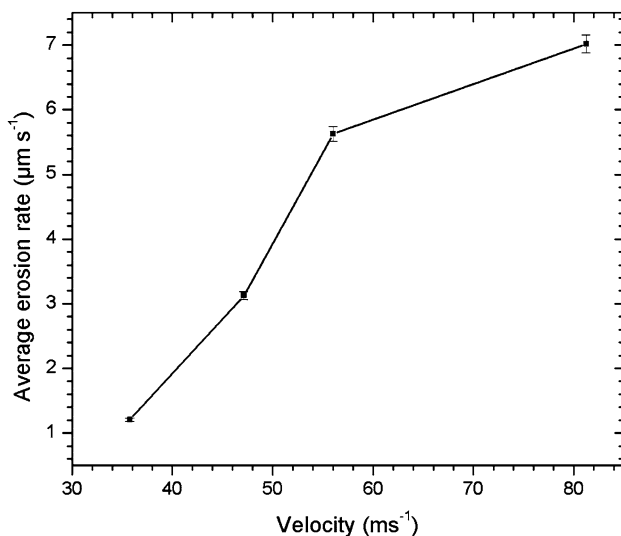


**Fig. 12** Average erosion rate vs particle velocity for API X42 steel during erosion–corrosion process. Each data point is an average of five erosion cycles

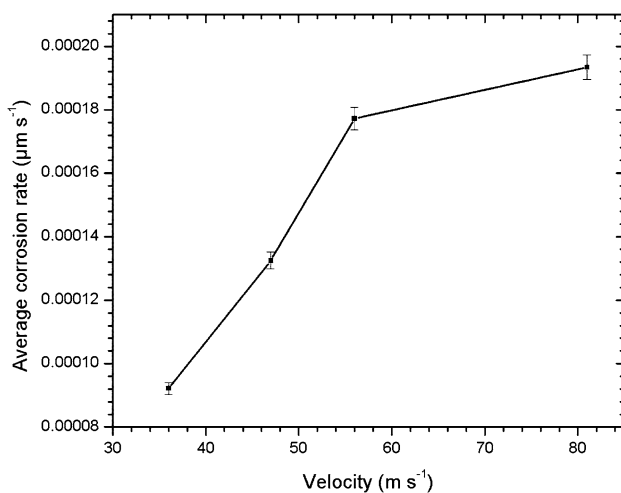


**Fig. 13** Average corrosion rate (based on weight loss) vs particle velocity for API X42 steel during erosion–corrosion test in which each data point is an average of five corrosion cycles

particle velocity leads to higher material removal creating more effective surface area for corrosion. Moreover, it is believed that due to high particle velocity, the sharp edges of the abrasive particles create micro-cracks and provide additional surface area for corrosion.

SEM micrographs of the API X42 steel after erosion–corrosion are shown in Fig. 14. Figure 14a shows the general surface morphology after the steel surface was exposed to five consecutive erosion–corrosion cycles (a total of 50 s erosion and 12.5 h corrosion). Synergistic effect between erosion and corrosion leads to high material removal during this process. A magnified image of Fig. 14a

(marked as circle) is shown in Fig. 14b. Upon impact, abrasive particles locally micro-forge the surface during the erosion cycle and form a work-hardened layer due to plastic deformation as observed in pure erosion. This work-hardened layer is highly susceptible to corrosion (more anodic) and experiences rapid corrosion during the corrosion cycle.

Al<sub>2</sub>O<sub>3</sub> particles are observed to embed into the steel surface and in some cases act as barriers and protect the surface underneath from corrosion. These embedded Al<sub>2</sub>O<sub>3</sub> particles may also act as nucleation sites for pits formation and surfaces adjacent to these embedded particles undergo preferential dissolution as shown in Fig. 14c. After sufficient dissolution (around the particles) in the same corrosion cycle, embedded particles are removed from the matrix and create fresh surfaces (cavities) for further corrosion. These cavities may act as initiation sites for pitting corrosion. Previous studies [102] showed that pits almost always initiate at some chemical and physical heterogeneity, such as second phase particles, inclusions, dislocations, and flaws. Figure 14d shows accelerated dissolution of iron inside the cavity where the adjacent surface area is protected by a corrosion film formed at the initial stage of corrosion.

Pits are often initiated at the steel surface (Fig. 14e) due to the breakdown of the passive film by the abrasive particles. These micro-sized pits are often considered as metastable pits and under certain conditions, they continue to grow to form large pits. These pits often covered with corrosion products [103], which make visual detection extremely difficult. Burstein [104] suggested that a cover over the pit mouth is required during a metastable state to maintain the diffusion controlled mechanism. Without the cover in this early growth stage, the pit would repassivate and die. Figure 14f shows the fracture of such pit cover during the erosion–corrosion process.

Figure 14g shows the fracture of Fe<sub>3</sub>C network by the abrasive particles. The damage to the Fe<sub>3</sub>C network significantly decreases the adherence of the protective surface film. Moreover, due to high particle velocity, the sharp edges of the abrasive particles create micro-cracks. During corrosion, corrosive solution penetrates through these cracks into the sub-surface region and extends these cracks further. Figure 14h shows the cross section of the specimen after erosion–corrosion illustrating the propagation of sub-surface crack. The propagation of sub-surface cracks during corrosion promotes delamination in the next erosion cycle.

Table 7 gives a summary of erosion–corrosion, pure erosion, and pure corrosion data (based on weight loss) for API X42 steel. Relative comparison of erosion and corrosion components (Fig. 15) indicates that the effect of

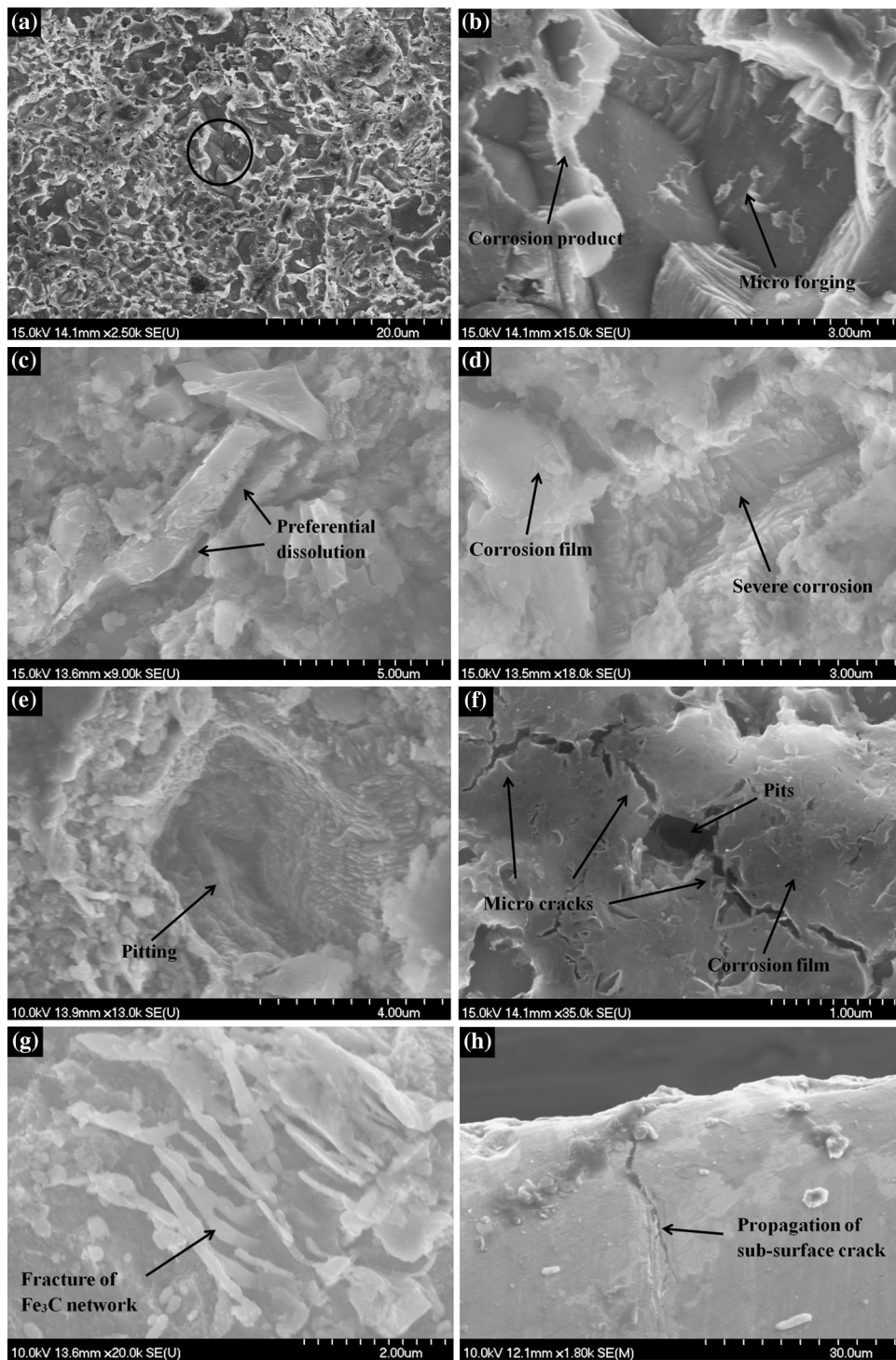


**Fig. 14** SEM micrographs of **a** surface morphology after erosion-corrosion, **b** magnified image of figure (a) (marked as circle) showing corrosion of work-hardened layer, **c** preferential dissolution of iron around an embedded particle, **d** accelerated corrosion inside a cavity, while the adjacent surface area is protected by a corrosion film,

**e** pitting corrosion due to the breakdown of passive film, **f** fracture of pit cover after sufficient growth of the pit underneath, **g** fracture of cementite network by abrasive particles during the erosion cycle and **h** cross section of the damaged surface showing propagation of sub-surface crack

corrosion on erosion and vice versa is significant. For 36, 47, 63, and 81 m s<sup>-1</sup> particle velocity, the increase in erosion rate due to corrosion is around 55, 15, 35, and

34 %, respectively. On the other hand, there are around 2, 3, 4, and 5 times increase in corrosion rate due to erosion for 36, 47, 63, and 81 m s<sup>-1</sup> particle velocity, respectively.

### 3.4 Effect of Corrosion on Erosion

Relative comparison of pure erosion and the total erosion component (due to erosion–corrosion) reveals that the effect of corrosion on erosion is significant. Surface roughness plays an important role during erosion. As described earlier, erosion is highly sensitive to impingement angle and an increase in surface roughness changes the local impact angle. Previous studies [73] showed that low angle metal cutting, plowing, and delamination predominate at low impingement angle leading to higher erosion rate. Moreover, increase in the surface roughness creates vulnerable local peaks, which are then easily removed during erosion. In this study, increase in surface roughness (around 54 %) due to corrosion causes higher erosion rate during erosion–corrosion.

It is believed that corrosion removes the work-hardened layer and exposes an unhardened surface for further erosion. At high impact angle (90°), extensive amount of Al<sub>2</sub>O<sub>3</sub> particles embed in the surface and act as reinforcing particles and slow down the erosion rate by protecting the underneath surface from additional erosion. However, preferential dissolution around the embedded particles (during the corrosion cycle) accelerates the removal of these embedded particles and increases the erosion rate by exposing fresh surface and creating vulnerable lips. Furthermore, due to high particle velocity, the sharp edges of the abrasive particle create micro-cracks during the erosion cycle. During the corrosion cycle, corrosive fluid penetrates and corrosion products precipitate inside the micro-cracks, which generates tensile stresses in front of the cracks leading to the extension of the cracks. The propagation of these micro-cracks promotes delamination in the next erosion cycle. Schematic diagram illustrating the propagation of micro-crack during the corrosion cycle is shown in Fig. 16.

As indicated in Table 7, the % increase in erosion rate due to corrosion decreases with increasing particle velocity (55, 15, 35, and 34 % for 36, 47, 63, and 81 m s<sup>-1</sup>, respectively). This indicates that the effect of corrosion on erosion is more pronounced at low particle velocity. This is mainly because, at high particle velocity, particles are embedded deep into the steel surface and work as barriers for further erosion. However, at low particle velocity, the particles are not embedded deep in the steel surface and can be easily removed by dissolution of the steel around these particles, hence, increasing the effect of corrosion on erosion. Moreover, high particle velocity creates thicker work-hardened layer and is not completely removed during the corrosion. It slows down the material loss rate during the erosion cycle.

A study by other researchers [105] suggested that although erosion rate depends on erosion mechanisms, the

**Table 7** Summary of erosion–corrosion data based on weight loss

Particle velocity	Total material loss ( <i>T</i> ) (μm s <sup>-1</sup> )	Total erosion component ( <i>E<sub>e</sub></i> ) (μm s <sup>-1</sup> )	Erosion rate in absence of corrosion ( <i>E<sub>0</sub></i> ) (μm s <sup>-1</sup> )	Total corrosion component ( <i>C<sub>c</sub></i> ) (μm s <sup>-1</sup> )	Corrosion rate in absence of erosion ( <i>C<sub>0</sub></i> ) (μm s <sup>-1</sup> )	Change in erosion rate due to corrosion (Δ <i>E<sub>e</sub></i> ) (μm s <sup>-1</sup> )	Change in corrosion rate due to erosion (Δ <i>C<sub>c</sub></i> ) (μm s <sup>-1</sup> )	% increase in erosion due to corrosion (Δ <i>E<sub>e</sub></i> / <i>E<sub>0</sub></i> )	% increase in corrosion due to erosion (Δ <i>C<sub>c</sub></i> / <i>C<sub>0</sub></i> )
36 m s <sup>-1</sup>	1.21	1.20	0.77	9.22 × 10 <sup>-5</sup>	3.80 × 10 <sup>-6</sup>	0.43	8.83 × 10 <sup>-5</sup>	55	2.3 × 10 <sup>3</sup>
47 m s <sup>-1</sup>	3.13	3.12	2.72	13.24 × 10 <sup>-5</sup>	3.80 × 10 <sup>-6</sup>	0.39	12.86 × 10 <sup>-5</sup>	15	3.3 × 10 <sup>3</sup>
63 m s <sup>-1</sup>	5.63	5.62	4.16	17.72 × 10 <sup>-5</sup>	3.80 × 10 <sup>-6</sup>	1.46	17.34 × 10 <sup>-5</sup>	35	4.4 × 10 <sup>3</sup>
81 m s <sup>-1</sup>	7.02	7.01	5.24	19.33 × 10 <sup>-5</sup>	3.80 × 10 <sup>-6</sup>	1.77	18.95 × 10 <sup>-5</sup>	34	4.9 × 10 <sup>3</sup>

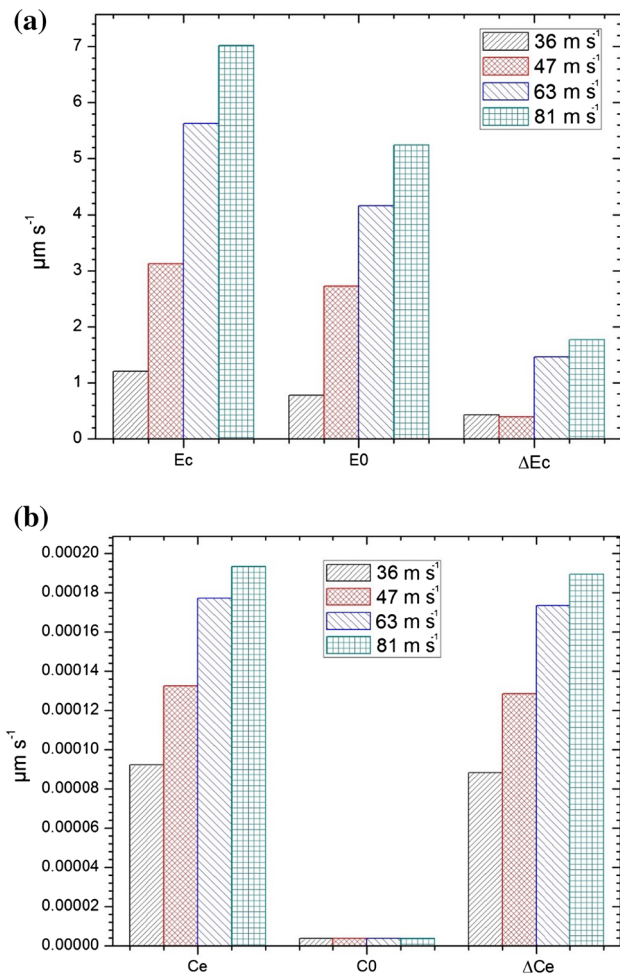


**Fig. 15** Relative comparison of **a** total erosion component, erosion rate in the absence of corrosion and change in erosion rate due to corrosion and **b** total corrosion component, corrosion rate in absence of erosion, and change in corrosion rate due to erosion

velocity exponent  $n$  is independent of erosion mechanisms and only depends on velocity and particle feed rate. However, at high particle feed rates such as the one employed in this study, the velocity exponent  $n$  decreases from 2.13 to 2.03 for pure erosion and erosion–corrosion, respectively. This indicates the dependency of erosion rate on velocity decreases and material loss rate becomes more dependent upon the mechanisms involved during the erosion–corrosion process.

### 3.5 Effect of Erosion on Corrosion

Significant increase in corrosion rate was observed during erosion–corrosion. This is mainly because the work-hardened layer formed after the erosion cycle is more anodic and makes the eroded surface highly susceptible to corrosion [85, 106]. Again, throughout the corrosion process, the precipitation of iron carbonate ( $\text{FeCO}_3$ ) forms a passive

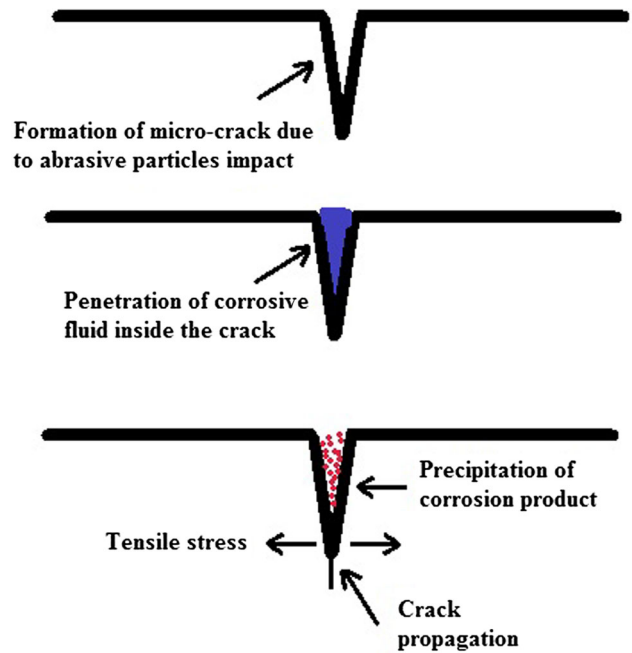


**Fig. 16** Schematic diagram showing the propagation of micro-crack during corrosion cycle. Precipitation of corrosion products inside the cracks generates tensile stress in front of the crack tip and extends the micro-cracks

film which acts as a diffusion barrier by covering the underlying metal and decreasing corrosion rate [101]. This layer is weakly bonded with the steel surface and easily removed (completely or partially) by erosive particles, which expose the fresh surface to the corrosive environment. Partial removal of the protective surface film creates favorable conditions for accelerated pitting corrosion. Additionally, disruptions in  $\text{Fe}_3\text{C}$  network in pearlite (due to erosion) significantly decrease the adherence of the protective film.

During erosion, abrasive particles are embedded within the matrix. These embedded particles act as nucleation sites for pit formation. Pits are often initiated on the steel surface due to the breakdown of passive film by the abrasive particles. Moreover, the increase in surface roughness due to abrasive particles impact increases the effective (real) surface area, which leads to higher corrosion rate [15, 16].

The effect of erosion on corrosion increases with increasing particle velocity. There are 2, 3, 4, and 5 times increase in corrosion rate due to erosion for 36, 47, 63, and 81  $\text{m s}^{-1}$  particle velocity, respectively. Higher particle velocity causes more damage to the passive film and exposes the fresh surface to the solution. Also, high velocity causes more embedded particles (creates more nucleation sites for pitting), more micro-cracks, and deeper penetration into the steel. After removal of these embedded particles, more effective surface area is exposed to the

corrosive media. Again, the thickness of the work-hardened layer increases with increasing particle velocity, which significantly increases the overall corrosion rate.

#### 4 Conclusions

In this study, sets of erosion, corrosion, and erosion–corrosion experiments were carried out on API X42 steel to evaluate synergistic effect between erosion and corrosion and to investigate possible degradation mechanisms. The following conclusions can be made from the current work:

- (1) In the course of the erosion at 90° angle of incidence, abrasive particles micro-forge the surface, induce heavy plastic deformation, and create work-hardened layer on the surface. Material removal occurs due to fracture and flattening of ridges around dimples.
- (2) Embedded abrasive particles reinforce the surface and slow down the erosion rate. Moreover, increasing particle velocity increases erosion rate. This is because the higher the impact velocity, the higher the kinetic energy, leading to heavier deformation and higher material removal.
- (3) During corrosion, preferential dissolution of eutectoid ferrite provides a suitable chemical environment for the formation of protective surface film on pearlite. Cementite ( $\text{Fe}_3\text{C}$ ) network in pearlite anchors the passive film to the surface.
- (4) Throughout the erosion–corrosion process, significant increase in erosion was observed due to corrosion. Corrosion increases surface roughness, removes work-hardened layer, and accelerates the removal of embedded particle. It also promotes delamination by extending sub-surface cracks.
- (5) Significant increase in corrosion was observed due to erosion. Erosion removes the passive film from the surface, breaks the cementite network, provides favorable conditions for pitting, and increases the effective surface area by increasing the surface roughness. In addition, erosion creates sub-surface cracks and deformed work-hardened layer, which increases corrosion kinetics.
- (6) The effect of corrosion on erosion is significant at low particle velocity, while the effect of erosion on corrosion is more prominent at high particle velocity.

**Acknowledgments** This publication was made possible by NPRP Grant no. 6-027-2-010 from the Qatar National Research Fund (a member of Qatar Foundation). The statements made herein are solely the responsibility of the authors. The authors would like to thank Mr. Dean Grijm and Mr. Syed Zakaria for their contributions.

#### References

1. Li Y, Burstein GT, Hutchings IM (1995) Influence of environmental composition and electrochemical potential on the slurry erosion-corrosion of aluminium. *Wear* 181–183:70–79
2. Hu X, Neville A (2005) The electrochemical response of stainless steels in liquid–solid impingement. *Wear* 258:641–648
3. Liang G, Peng X, Xu L, Cheng YF (2013) Erosion-corrosion of carbon steel pipes in oil sands slurry studied by weight-loss testing and CFD simulation. *J Mater Eng Perform* 22:3043–3048
4. Aribio S, Bryant M, Neville A, Hu X (2013) Erosion-corrosion of lean duplex stainless steel (UNS S32101) in a CO<sub>2</sub>-saturated oilfield brine, corrosion (2013) Paper ID 2382, NACE International, Orlando
5. Macdonald DD, Cragolino GA (1989) Corrosion of steam cycle materials, ASME handbook on water technology for thermal power systems, Vol. 8, Chapter 9. ASME, New York
6. Li Y, Burstein GT, Hutchings IM (1995) The influence of corrosion on the erosion of aluminium by aqueous silica slurries. *Wear* 186–187:515–522
7. Wood RJK (2006) Erosion-corrosion interactions and their effect on marine and offshore materials. *Wear* 261:1012–1023
8. Zhao GX, Hong X, Xiang JM, Han Y (2009) Formation characteristic of CO<sub>2</sub> corrosion product layer of P110 steel investigated by SEM and electrochemical techniques. *J Iron Steel Res Int* 16:89–94
9. Ogundele GI, White WE (1986) Some observation on corrosion of carbon steel in aqueous environments containing carbon dioxide. *NACE* 42:71–78
10. Guo XP, Tomoe Y (1999) The effect of corrosion product layers on the anodic and cathodic reactions of carbon steel in CO<sub>2</sub>-saturated MDEA solutions at 100 & #xB0;C. *Corros Sci* 41(7):1391–1399
11. Amri J, Gulbrandsen E, Nogueira RP (2008) The effect of acetic acid on the pit propagation in CO<sub>2</sub> corrosion of carbon steel. *Electrochem Commun* 10(2):200–203
12. Faysal FE, Mahdi ES, Akram A (2012) Electrochemical evaluation of the corrosion behaviour of API-X100 pipeline steel in aerated bicarbonate solutions. *Corros Sci* 58:181–191
13. Villarreal J, Laverde D, Fuentes C (2006) Carbon-steel corrosion in multiphase slug flow and CO<sub>2</sub>. *Corros Sci* 48(9):2363–2379
14. Stack M, Abdulrahman GH (2012) Mapping erosion-corrosion of carbon steel in oil–water solutions: effects of velocity and applied potential. *Wear* 274–275:401–413
15. Zhang GA, Cheng YF (2009) Electrochemical corrosion of X65 pipe steel in oil/water emulsion. *Corros Sci* 51:901–907
16. Tang X, Xu LY, Cheng YF (2008) Electrochemical corrosion behavior of X-65 steel in the simulated oil–sand slurry. II: synergism of erosion and corrosion. *Corros Sci* 50:1469–1474
17. Hassani S, Roberts KP, Shirazi S, Shadley JR, Rybicki EF, Joia C (2013) A New Approach for predicting inhibited erosion-corrosion in CO<sub>2</sub>-saturated oil/brine flow condition. *SPE Prod Oper* 28:135–144
18. Saleh B, Ahmed SM (2013) Slurry erosion-corrosion of carburized AISI 5117 steel. *Tribol Lett* 51:135–142
19. Dou YH, Li Y, Wang ZG, Li Z (2013) Study of the erosion-corrosion behavior of P110, N80 and VM140 steel in 3.5 wt% NaCl solutions with sand. *Adv Mater Res* 683:353–356
20. Postlethwaite J (1981) Effect of chromate inhibitor on the mechanical and electrochemical components of erosion-corrosion in aqueous slurries of sand. *Corrosion* 37(1):1–9



21. Matsumura M, Oka Y, Hiura H, Yano M (1991) The role of passivating film in preventing slurry erosion-corrosion of austenitic stainless steel. *SII Int* 31(2):168–176
22. Hu X, Neville A (2009) CO<sub>2</sub> erosion-corrosion of pipeline steel (API X65) in oil and gas conditions—a systematic approach. *Wear* 267:2027–2032
23. Stack MM, Zhou S, Newman RC (1995) Identification of transitions in erosion-corrosion regimes in aqueous environments. *Wear* 186–187:523–532
24. Malka R, Srdjan N, Gulino D (2007) Erosion-corrosion and synergistic effects in distributed liquid-particle flow. *Wear* 262:791–799
25. Yabuki A, Matsuwaki K, Matsumura M (1999) Critical impact velocity in the solid particles impact erosion of metallic materials. *Wear* 233–235:468–475
26. Liebhart M, Levy A (1991) The effect of erodent particle characteristics on the erosion of metals. *Wear* 151:381–390
27. Divakar M, Agarwal VK, Singh SN (2005) Effect of the material surface hardness on the erosion of AISI 316. *Wear* 259:110–117
28. Clark H, Hartwich RB (2001) A re-examination of the ‘particle size effect’ in slurry erosion. *Wear* 248:147–161
29. ElTobgy MS, Elbestawi MA (2005) Finite element modeling of erosive wear. *Int J Mach Tools* 45:1337–1346
30. Wood RJK, Jones TF (2003) Investigations of sand–water induced erosive wear of AISI 304L stainless steel pipes by pilot-scale and laboratory-scale testing. *Wear* 255:206–218
31. Levy A, Chik P (1983) The effects of erodent composition and shape on the erosion of steel. *Wear* 89:151–162
32. Stachwick GW, Batchelor AW (2001) *Engineering tribology*, 2nd edn. Butterworth-Heinemann, Boston
33. Finnie I, Stevick GR, Ridgely JR (1992) The influence of impingement angle on the erosion of ductile metals by angular abrasive particles. *Wear* 152:91–98
34. Oka YI, Ohnogi H, Matsumura M (1997) The impact angle dependence of erosion damage caused by solid particle impact. *Wear* 203–204:573–579
35. Finnie I (1958) The mechanism of erosion of ductile metals, 3rd U.S. national congress of applied mechanics. ASME, New York, pp 527–532
36. Bitter JGA (1963) A study of erosion phenomena: part I. *Wear* 6:5–21
37. Bitter JGA (1963) A study of erosion phenomena: part II. *Wear* 6:169–190
38. Hutchings IM (1992) *Tribology: friction and wear of engineering materials*. Edward Arnold, London
39. Hutchings IM (1981) A model for the erosion of metals by spherical particles at normal incidence. *Wear* 70:269–281
40. Levy AV (1986) The platelet mechanism of erosion of ductile metals. *Wear* 108:1–21
41. Lopez D, Congote JP, Cano JR, Toro AP, Tschiptschin AP (2005) Effect of particle velocity and impact angle on the corrosion–erosion of AISI 304 and AISI 420 stainless steels. *Wear* 259:118–124
42. Tilly GP (1973) A two stage mechanism of ductile erosion. *Wear* 23:87–96
43. Stevenson ANJ, Hutchings IM (1995) Scaling laws for particle velocity in the gas-blast erosion test. *Wear* 181–183:56–62
44. Desale GR, Gandhi BK, Jain SC (2008) Slurry erosion of ductile materials under normal impact condition. *Wear* 264:322–330
45. Molinari JF, Ortiz M (2002) A study of solid-particle erosion of metallic targets. *Int J Impact Eng* 27:347–358
46. Mbabazi JG, Sheer TJ, Shandu R (2004) A model to predict erosion on mild steel surfaces impacted by boiler fly ash particles. *Wear* 257:612–624
47. Akbarzadeh E, Elsaadawy E, Sherik AM, Spelt JK, Papini M (2012) The solid particle erosion of 12 metals using magnetite erodent. *Wear* 282–283:40–51
48. Deng T, Chaudhry AR, Patel M, Hutchings I, Burnett AJ (2001) Effect of particle concentration on erosion rate of mild steel bends in a pneumatic conveyor. *Wear* 248:162–177
49. Tilly GP, Sage W (1970) The interaction of particle and material behaviour in erosion process. *Wear* 16:447–465
50. Shipway PH, Hutchings IM (1994) A method for optimizing the particle flux in erosion testing with a gas-blast apparatus. *Wear* 174:169–175
51. Anand K, Hovis SK (1987) Flux effects in solid particle erosion. *Wear* 118:243–257
52. Liebhart M, Levy A (1991) The effect of erodent particle characteristics on the erosion of metals. *Wear* 151:381–390
53. Palacios CA, Shadley JR (1991) Characteristics of corrosion scales on steels in a CO<sub>2</sub>-saturated NaCl brine. *Corrosion* 47:122–127
54. Dayalan E, de Moraes FD, Shadley JR, Rybicki EF, Shirazi SA (1998) CO<sub>2</sub> corrosion prediction in pipe flow under FeCO<sub>3</sub> scale-forming conditions. *Corrosion* 98:22–27 March, San Diego, California
55. Wang C, Neville A, Ramachandran S, Jovancicevic V (2005) Alleviation of erosion–corrosion damage by liquid–sand impact through use of chemicals. *Wear* 258:649–658
56. Dayalan E, Vani G, Shadley JR, Shirazi SA, Rybicki EF (1995) Modelling CO<sub>2</sub> corrosion of carbon steel in pipe flow, *Corrosion/95*, paper no. 118 (Houston, TX: NACE International)
57. Lide DR (1998–1999) (ed) 79th edn. *Handbook of chemistry and physics*. CRS Press, Boca Raton
58. Stack MM, Jana BD (2004) Modelling particulate erosion-corrosion in aqueous slurries: some views on the construction of erosion-corrosion maps for a range of pure metals. *Wear* 256:986–1004
59. Tian BR, Cheng YF (2008) Electrochemical corrosion behaviour of X-65 steel in the simulated oil sand slurry. I. Effects of hydrodynamic condition. *Corros Sci* 50:773–779
60. Sasaki K, Burstein GT (2007) Erosion-corrosion of stainless steel under impingement by a fluid jet. *Corros Sci* 49(1):92–102
61. Gnanavelu A, Kapur N, Neville A, Flores JF (2009) An integrated methodology for predicting material wear rates due to erosion. *Wear* 267(11):1935–1944
62. Neville A, Wang C (2009) Erosion-corrosion mitigation by corrosion inhibitors—an assessment of mechanisms. *Wear* 267(1–4):195–203
63. Rajahram SS, Harvey TJ, Wood RJK (2011) Electrochemical investigation of erosion-corrosion using a slurry pot erosion tester. *Tribol Int* 44(3):232–240
64. Rajahram SS, Harvey TJ, Wood RJK (2010) Full factorial investigation on the erosion-corrosion resistance of UNS S31603. *Tribol Int* 43(11):2072–2083
65. ASTM. G119-09 (2009), Standard guide for determining synergism between wear and corrosion, Annual Book of ASTM Standards, Vol 03.02, ASTM International, West Conshohocken, PA
66. Stack MM, Pungwiwat N (2004) Erosion-corrosion mapping of Fe in aqueous slurries: some views on a new rationale for defining the erosion-corrosion interaction. *Wear* 256:565–576
67. G76 – 07: Standard test method for conducting erosion tests by solid particle impingement using gas jets, ASTM International
68. Mohyaldinn ME, Elkhatib N, Ismail MC (2013) *Wear of pipe components due to sand production with oil and gas*. Lambert Academic Publishing, New York
69. ISO 13320 (2009) Particle size analysis—laser diffraction methods, International Organization for Standardization

70. Chang LC, Hsui IC, Chen LH, Lui TS (2005) A study on particle erosion behavior of ductile irons. *Scripta Mater* 52:609–613
71. Ian M (1992) Hutchings, ductile-brittle transitions and wear maps for the erosion and abrasion of brittle materials. *J Phys D Appl Phys* 25:A212–A221
72. Ruff AW, Ives LK (1975) Measurement of solid particle velocity in erosive wear. *Wear* 35:195–199
73. Islam MA, Farhat Z, Ahmed E, Alfantazi AM (2013) Erosion enhanced corrosion and corrosion enhanced erosion of API X70 pipeline steel. *Wear* 302:1592–1601
74. Islam MA, Farhat Z (2014) Effect of impact angle and velocity on erosion of API X42 pipeline steel under high abrasive feed rate. *Wear* 311:180–190
75. ASTM. G 59–97 (2009), Standard test method for conducting potentiodynamic polarization resistance measurements, Annual Book of ASTM Standards, Vol 03.02, ASTM International, West Conshohocken, PA
76. Shadley JR, Shirazi SA, Dayalan E, Rybicki EF (1996) Erosion-corrosion of a carbon steel elbow in a carbon dioxide environment. *Corrosion* 52:714–723
77. Shadley JR, Shirazi SA, Dayalan E, Rybicki EF (1998) Prediction of erosion-corrosion penetration rate in a carbon dioxide environment with sand. *Corrosion* 54:972–978
78. Hu X, Neville A (2008) Prediction of erosion-corrosion in oil and gas—a systematic approach, NACE International, Corrosion New Orleans, Louisiana, Paper no. 08540
79. Wang C, Neville V (2004) Understanding the action of inhibitors in mitigating erosion-corrosion in impinging flows, NACE International, Corrosion, New Orleans, Louisiana, Paper no. 04658
80. Hu X, Neville A (2004) An examination of the electrochemical characteristics of two stainless steels (UNS S32654 and UNS S31603) under liquid–solid impingement. *Wear* 256:537–544
81. Hu X, Barker E, Neville A, Gnanavelu A (2011) Case study on erosion-corrosion degradation of pipework located on an off-shore oil and gas facility. *Wear* 271:1295–1301
82. Stack MM, Abdulrahman GH (2012) Mapping erosion-corrosion of carbon steel in oil-water solutions: effects of velocity and applied potential. *Wear* 274–275:401–413
83. Rajahram SS, Harvey TJ, Wood RJK (2009) Erosion-corrosion resistance of engineering materials in various test conditions. *Wear* 267:244–254
84. Harvey TJ, Wharton JA, Wood RJK (2007) Development of synergy model for erosion-corrosion of carbon steel in a slurry pot. *Tribol Mater Surf Interfaces* 1:33–47
85. Xie J, Alpas A, Northwood D (2003) Mechano-electrochemical effect between erosion and corrosion. *J Mater Sci* 38:4849–4856
86. Lopez D, Congote JP, Cano JR, Toro AP, Tschiptschin AP (2005) Effect of particle velocity and impact angle on the corrosion-erosion of AISI 304 and AISI 420 stainless steels. *Wear* 259:118–124
87. Sundararajan G (1991) The depth of plastic deformation beneath eroded surfaces: the influence of impact angle and velocity, particle shape and material properties. *Wear* 149:129–153
88. Levy AV (1986) The platelet mechanism of erosion of ductile metals. *Wear* 108:1–21
89. Oka Y, Matsumura M, Kawabata T (1993) Relationship between surface hardness and erosion damage caused by solid particle impact. *Wear* 162:688–695
90. Islam MA, Farhat ZN (2012) The synergistic effect between erosion and corrosion of API pipeline in CO<sub>2</sub> and saline medium. *Tribol Int* 68:26–34
91. Wood RJK, Walker JC, Harvey TJ, Wang S, Rajahram SS (2013) Influence of microstructure on the erosion and erosion-corrosion characteristics of 316 stainless steel. *Wear* 306:254–262
92. Hutchings IM, Winter RE, Field JE (1976) Solid particle erosion of metals: the removal of surface material by spherical projectiles. *Proc R Soc Lond A* 348:379–392
93. Deng T, Bingley MS, Bradley MSA (2004) The influence of particle rotation on the solid particle erosion rate of metals. *Wear* 256:1037–1049
94. Mora-mendoza JL, Turgoose S (2002) Fe<sub>3</sub>C influence on the corrosion rate of mild steel in aqueous CO<sub>2</sub> systems under turbulent flow conditions. *Corros Sci* 44:1223–1246
95. Al-hasan S, Mishra B, Olson DL, Salama MM (1998) Effect of microstructure on corrosion of steels in aqueous solution containing carbon dioxide. *Corrosion* 54:480–491
96. Dugstad A, Hemmer H, Seiersten M (2001) Effect of steel microstructure on corrosion rate and protective iron carbonate film formation. *Corrosion* 57:369–378
97. Ogundele GI, White WE (1986) Some observations on corrosion of carbon steel in aqueous environments containing carbon dioxide. *Corrosion* 42:71–78
98. Heuer JK, Stubbings JF (1999) An XPS characterization of FeCO<sub>3</sub> films from CO<sub>2</sub> corrosion. *Corros Sci* 41:1231–1243
99. Heuer JK, Stubbings JF (1998) Microstructure analysis of coupons exposed to carbon dioxide corrosion in multiphase flow. *Corrosion* 54:566–575
100. Palacios CA, Shadley JR (1991) Characteristics of corrosion scales on steels in a CO<sub>2</sub> saturated NaCl brine. *Corrosion* 47:122–127
101. Nordsveen M, Nestic S, Nyborg R, Stangeland A (2003) A mechanistic model for carbon dioxide corrosion of mild steel in the presence of protective iron carbonate films—Part 1: theory and verification. *Corros Sci* 59:443–456
102. Szklarska-Smialowska Z (1986) Pitting corrosion of metals. NACE International, Houston
103. Frankel GS, Stockert L, Hunkeler F, Boehni H (1987) Metastable pitting of stainless steel. *Corrosion* 43:429–436
104. Sasaki K, Burstein GT (1996) The generation of surface roughness during slurry erosion-corrosion and its effect on the pitting potential. *Corros Sci* 38:2111–2120
105. Lindsley BA, Marder AR (1999) The effect of velocity on the solid particle erosion rate of alloys. *Wear* 225–229:510–516
106. Xie J, Alpas A, Northwood D (2003) The effect of erosion on the electrochemical properties of AISI 1020 steel. *J Mater Eng Perform* 12(2003):77–86